Journal of Computer Assisted Tomography
24(1):128–138

Analyzing Functional Brain Images in a Probabilistic Atlas: A Validation of Subvolume Thresholding

Ivo D. Dinov, Michael S. Mega, Paul M. Thompson, Linda Lee, Roger P. Woods, Colin J. Holmes, De Witt L. Sumners, and Arthur W. Toga

Purpose: The development of structural probabilistic brain atlases provides the framework for new analytic methods capable of combining anatomic information with the statistical mapping of functional brain data. Approaches for statistical mapping that utilize information about the anatomic variability and registration errors of a population within the Talairach atlas space will enhance our understanding of the interplay between human brain structure and function.

Method: We present a subvolume thresholding (SVT) method for analyzing positron emission tomography (PET) and single photon emission CT data and determining separately the statistical significance of the effects of motor stimulation on brain perfusion. Incorporation of a priori anatomical information into the functional SVT model is achieved by selecting a proper anatomically partitioned probabilistic atlas for the data. We use a general Gaussian random field model to account for the intrinsic differences in intensity distribution across brain regions related to the physiology of brain activation, attenuation effects, dead time, and other corrections in PET imaging and data reconstruction.

Results: $H_2{}^{15}O$ PET scans were acquired from six normal subjects under two different activation paradigms: left-hand and right-hand finger-tracking task with visual stimulus. Regional region-of-interest and local (voxel) group differences between the left and right motor tasks were obtained using nonparametric stochastic variance estimates. As expected from our simple finger movement paradigm, significant activation ($z = 6.7$) was identified in the left motor cortex for the right movement task and significant activation ($z = 6.3$) for the left movement task in the right motor cortex.

Conclusion: We propose, test, and validate a probabilistic SVT method for mapping statistical variability between groups in subtraction paradigm studies of functional brain data. This method incorporates knowledge of, and controls for, anatomic variability contained in modern human brain probabilistic atlases in functional statistical mapping of the brain.

Index Terms: Atlas and atlases—Brain, anatomy—Maps and mapping—Single photon emission computed tomography (SPECT)—Emission computed tomography.

Through parallel efforts at multiple neuroimaging centers, the goal of constructing population-based probabilistic atlases (1) of the human brain is being realized. The need to improve on a single brain-based atlas system, such as the Talairach atlas (2), is motivated by a necessity to account for morphologic variability in brain anatomy across normal and diseased populations (3–6). Incorporating information about anatomic variability within these new atlases requires new statistical techniques that integrate that variability in the assessment of functional imaging data. The International Consortium of Human Brain Mapping (ICBM) has constructed a probabilistic human brain atlas derived from young normal subjects (3), which now permits the testing of statistical mapping algorithms designed to answer the present, and future, functional brain-mapping needs.

We demonstrate a robust technique for modeling and analysis of positron emission tomography (PET) data using a probabilistic 3D atlas reflecting anatomical, geometrical, and functional aspects of the brain systems un-

From the Laboratory of Neuro Imaging, Department of Neurology, University of California at Los Angeles, Los Angeles, CA (I. D. Dinov, M. S. Mega, P. M. Thompson, L. Lee, R. P. Woods, C. J. Holmes, and A. W. Toga), and Department of Mathematics, Florida State University, Tallahassee, FL (D. W. L. Sumners), U.S.A. Address correspondence and reprint requests to Dr. A. W. Toga at Laboratory of Neuro Imaging, Department of Neurology, 710 Westwood Plaza, University of California at Los Angeles, Los Angeles, CA 90095-1769, U.S.A.

der study (3,7). Following a statistical analysis of global activation, we apply local statistical significance tests to each voxel intensity within the globally activated regions of interest (ROIs) according to the preceding global analysis.

Our method uses multiple scans of the same or different subject(s) and determines appropriate threshold value(s) for different regions of the brain depending on their size and geometry. It also uses a general stationary random field modeling of the noise factor so that every probabilistically defined region is studied separately.

Signal variance estimates are the foundation of the analysis for determining the statistically significant changes of functional activity. In functional imaging, there are at least five major sources of error in variance estimates (8): first, spatial brain-positioning differences between the activation and the baseline scans; second, using an inadequate statistical model; third, differences in global activity in various regions of the brain; fourth, the effects of intersubject intensity variability (for multiple subject studies); and finally, the limited resolution of the imaging equipment (8).

In the subvolume thresholding (SVT) technique, the above potential errors are addressed as follows: Probabilistically defined ROIs will control for small local morphological (structural) differences between activation and baseline images for the corresponding ROI after a rigid-body, affine, or nonaffine warp is performed (9). Modeling the signal in different ROIs as separate stationary random fields accommodates nonuniform global activity within the brain. The ROIs, mapped as probabilistic (cloud-like) fields, anatomically partition the target atlas. In this article, we consider subtraction paradigms, where one seeks to identify and interpret differences between two groups of subjects divided by their activation stimuli. To estimate the variance of the difference data, we use a dual (hybrid) longitudinal-meridianal approach; variance is pooled across subjects and across voxels. Differences in global activity between groups are resolved by intensity normalization. This equalizes the means of the functional data across subjects. Last, the smearing effects of the PET cameras are accommodated by adopting a Gaussian random field model. The blurring of PET imaging devices can be accurately modeled by a normal smoothing filter with certain (measurable) variance related to the full width at half-maximum (FWHM) (10).

Given the development of current and future probabilistic atlases for various populations, we have developed a new statistical mapping procedure for functional imaging data that incorporates the anatomical information contained in these brain atlases. We validate the SVT technique with a simple finger-moving task.

METHODS

In our study, we have employed a probabilistic partitioning based on the ICBM atlas (3). This stereotactic human brain atlas was produced using 305 normal subjects (25–35 years old) and includes the following nine ROIs: the cerebellum, the left and right frontal, occipital, parietal, and temporal lobes, putamen, caudate, insula, and thalamus. A probability map was assigned to every voxel in each ROI, or subvolume, that reflects the chance that on average this voxel location falls within the ROI. Thus, each ROI is a cloud-like structure with probabilities of 1 deep inside the subvolume and decreasing probabilities associated with voxels toward the ROI boundary. Figure 1 shows sagittal, coronal, and axial views of these structures.

Data Acquisition with Preprocessing

Informed consent was obtained from all subjects, and the study protocol was reviewed and approved by the UCLA Human Subject Protection Committee. $H_2{}^{15}O$ blood flow PET data were acquired from six normal volunteers using a Siemens/CTI 831-08 tomograph (Siemens, Hoffman Estates, IL, U.S.A.) under a left- and right-hand finger-tracking task with visual stimulus (11). The PET camera generated eight direct planes and seven cross-planes with an interplane distance of 6.75 mm for each volumetric data set. The six subject were scanned twice for each motor task using 10 mCi/injection of $H_2{}^{15}O$. The stereotactic 3D PET data were reconstructed using a Shepp reconstruction filter with a roll-off frequency of 0.16 mm^{-1}, resulting in volumes with FWHM of 6.1 mm. Attenuation corrections of $\mu = 0.151$ cm^{-1} for skull and $\mu = 0.095$ cm^{-1} for soft tissue were used for the reconstruction. The axial data dimensions were

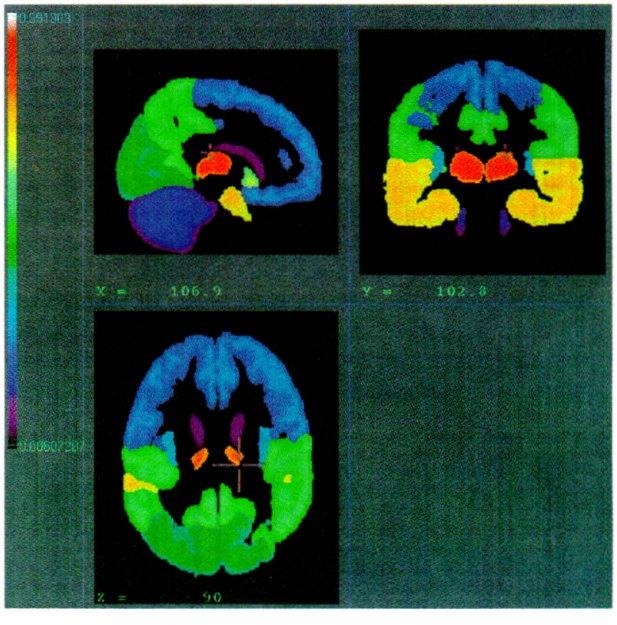

FIG. 1. Nine probabilistically defined regions of interest: part of the International Consortium of Human Brain Mapping anatomic atlas.

$128 \times 128 \times 55$ pixels with pixel size of 1.75 mm. The corresponding reconstructed volumes were aligned to one of them, randomly selected, using an affine 12 parameter automated algorithm (9). Then, the average of the 12 prealigned PET volumes were registered to the ICBM atlas (3), again by a 12 parameter affine registration. Combining the warping fields, with a single reslicing, all the data were registered in ICBM space. Finally, a global (linear) intensity normalization was performed within each of the two groups to equalize the overall means of the PET data.

Subvolume Thresholding

For notational purposes let X^1_a and X^2_r, for $1 \leq a,r > N$, represent the coregistered observed (functional) data of the subjects in the two groups of interest, paradigm 1 (left-hand finger tracking) versus paradigm 2 (right-hand finger tracking). More precisely, $X^1_a = X^1_{a,(i,j,k)}$ and $X^2_r = X^2_{r,(i,j,k)}$ on a 3D grid of voxels.

Let $D_l = X^1_l - X^2_l$ ($D_l = D_{l,(i,j,k)}$) be the lth randomly paired difference data. Suppose also that we impose an anatomically relevant partitioning on the common domain of our functional data after spatial registration. We think of the spatial domain of the data, Dom(D), as being a disjoint union of subsets, $\text{Dom}(D) = \cup_{m=1}^{M} \text{Dom}(D^m)$ (Fig. 2). Depending on the particular hypothesis, a partitioning scheme may be selected in which domain subsets are topologically connected or disconnected. The latter case is applicable for studying regions only functionally connected. For example, attenuation effects, dead time, and other corrections in PET or single photon emission CT (SPECT) imaging and data reconstruction lead to differences in voxel variances between the white matter and grey matter. Thus, one may adopt a proper brain segmentation procedure to analyze statistical significance over the three tissue types differently, exploiting the intrinsic differences in voxel variability. The reader may think of the domains of the partitioned subimages as rectangles or parallelepipeds (in 2D and 3D, respectively).

The SVT technique determines whether there are statistically significant differences between two groups of data within each ROI, or subdomain D^m, and, if so, proceeds to locate the activation sites (voxels).

First, consider one separate subdomain, D^m. Neighboring voxel intensities in functional imaging are highly correlated due to imperfect resolution of the imaging equipment, noise effects, and the physiology of brain activation. We assume that a Gaussian autocorrelation function governs this spatial intensity dependence. Moreover, we assume that in a subtraction paradigm study, the autocorrelation of the voxel intensities in two different subjects is independent of the ordering of the subjects within each group. Let the effective spatial resolution of the scanner, WHM (12), in dimension i be σ_{s_i} mm, the voxel size in dimension i be x_i mm, $\sigma_s = \max\{\sigma_{s_i}\}\ 1 \leq i \leq 3$, and $x = \min\{x_i\}\ 1 \leq i < 3$. Then two intensities, at voxel locations v_1 and $v_1 + h$, $h \in R^3$, are not significantly correlated if the distance between them is $d(v_1, v_1 + h) \geq h_0 = [\sigma_s/x]$, where $[\bullet]$ is the greatest integer function [$\text{Cov}(D_{v_1}, D_{v_1+h}) \leq K\rho^{h_0}$, for some $0 < \rho < 1$]. Voxels farther apart than the FWHM may be regarded as uncorrelated. Let $\|h\|_p^p = \Sigma_i |h|^p$, for $p = 1, 2, 3, \ldots$ be the regular p norm on R^3. For the covariance model we discuss later, $\text{Cov}(D_{v_1}, D_{v_1+h}) = c(h) = K\rho^{\|h\|_p^p} = Ke^{-\|h\|_p^p \ln(1/\rho)}$, we can derive a relationship between the spread (FWHM) of the Gaussian autocorrelation and the parameter ρ. Let $h_1 = 3\ [2\ \ln(1/\rho)]^{-1}$; then correlation between voxels v_1 and $v_1 + h$ is small if $h_1 \approx h_0$. This equation depicts an approximate relation between ρ and σ_s: $\rho \approx e^{-3/2h_0}$. The larger the σ_s, the smaller ρ and the larger the size of the Gaussian smoothing kernel. Conversely, the smaller σ_s, the larger ρ and the smaller the autocorrelation spreading kernel. In the present PET motor activation study, all data have been affinely registered and analyzed in the common anatomical ICBM space (3), where the voxel size is $1 \times 1 \times 1$ mm^3, the maximal FWHM (σ_s) of the PET camera is 6 mm, and the kernal parameter $\rho \approx e^{-1/4} = 0.77880078$. In general, for nonisotropic FWHMs, one can use the (positive definite) tensor $T = (\sigma_{s_1}\ 0\ 0/0\ \sigma_{s_2}\ 0/0\ 0\ \sigma_{s_3})$ to define a metric $\|h\|_0^2 = h^T T^{-1} h$. Then the covariogram becomes $\text{Cov}(D_{x_1}, D_{x_1+h}) = K\rho^{\|h\|_0^2}$, which allows for a more flexible model.

A reasonable estimate[1] of the variance of the difference data over D^m, $\sigma^2_{D^m}$ is the subsample variance of a random collection of voxels (I) within the domain Dom(D^m) that are far enough apart from each other to be spatially uncorrelated (see below). These random voxels are chosen according to the underlying anatomic probability distribution associated with the particular ROI:

$$\widehat{\sigma^2_{D^m}} = \frac{1}{N \times |I|} \sum_{\substack{x \in I \\ 1 \leq l \leq N}} [D_l^m(x) - \overline{D^m}]^2$$

where

$$\overline{D^m} = \frac{1}{N \times |I|} \sum_{\substack{x \in I \\ 1 \leq l \leq N}} D_l^m(x)$$

FIG. 2. Geometric **(left),** specific anatomic or anatomic average **(middle),** and probabilistic **(right)** partitioning schemes.

[1] The common "hat" notation, ^, is used for estimated quantities.

Under normal assumptions, for voxel intensities, we do voxel-wise z tests (for $x \in D^m$):

$$z_x = \frac{1/N \sum_{l=1}^{N} D_l^m(x)}{\widehat{\sigma_{D^m}}}$$

to determine the location of the statistically significant sites of activation within D^m. Note that the normal assumption for z_x is usually justified because of the large degrees of freedom. If this is not the case, one typically employs standard t testing.

Because of the large number of tests (the number of voxels within a search region may be larger than 2^{18}), we will correct for the increasing false-positive test error by testing at a significance level $\alpha_0 = \alpha/|I|$, where $|I|$ is the approximate number of voxels (within the search region) that are uncorrelated (farther apart than $2 \times$ FWHM). The initial significance level is set at $\alpha = 0.05$. To correct for inhomogeneity of the subtraction data across different brain regions and for multiple comparisons, we employ a twofold approach: First, we determine if there is a need to conduct a voxel-by-voxel search for activation inside Dom(D^m) by identifying the regions Dom(D^m) in which global activation is present at $\alpha = 0.05$ The globally activated subvolumes D^m will then be the only domains subjected to the second local search. We begin by estimating the standard deviatioin of the sample average within a selected subvolume,

$$\overline{D^m} = \frac{1}{N \times n_{\text{tot}}} \sum_{\substack{x \in D^m \\ 1 \le l \le N}} D_l^m(x)$$

where n_{tot} is the total number of voxels in the domain of the subvolume D^m. Using the standard error $\sigma_{\overline{D}^m}$, we test the subvolume D^m, as a whole entity, for activation significance.

Our model includes three fundamental assumptions. The first is that neighboring sites (voxels) have Gaussian autocorrelation depending on the distance between them. This assumption is sometimes violated (13,14) due to negative side lobes in the x,y plane and frequency-space truncation filtering in the process of PET image reconstruction. The second implicit assumption is that under the null hypothesis, the intensities at every voxel of the difference images are normally distributed with mean zero and some unknown variance. The last hypothesis is that the autocorrelation function of the intensities at two locations (x_1 and x_2) of two different subjects does not depend on the choice of the subjects within each group. Hence, the covariogram $\text{Cov}[D_l(x_1), D_k(x_2)]$ is invariant under the action of the group of permutations on the subject indexes k and l. This assumption is natural because if the autocorrelation function does depend on the subject indexes, then it will depend on the ordering of the subjects in each group that will make our final group statistical significance maps heavily dependent on position of the subjects within each group. Such a conclusion would clearly jeopardize the validity and uniqueness of the results. Therefore, the autocorrelation function of the model has the property

$$\text{Cov}[D_l(x_1), D_k(x_2)] = \text{Cov}[D_1(x_1), D_1(x_2)] = K\rho^{d(x_1,x_2)}$$

for any l and k, where $d(x_1, x_2)$ is a distance function on R^3. In Appendix, we show that the other two assumptions are reasonable.

Estimates of Variances

For simplicity of notation, we will be suppressing the superindex m and regard D^m as a whole new image, D. Assume that our data is a stationary Gaussian n-dimensional random field D_x (15), where $n = 2,3$ for 2D or 3D image data. Then D has constant (across-voxel) mean $E(D_x) = \mu = \text{const}$, for all $x \in R^n$ and a spatial autocorrelation functioin of the form $\text{Cov}(D_{x_1}, D_{x_2}) = C(x_1, x_2) = c(x_1 - x_2)$, where $c : R^n \to R$. Let $x_1 = (i_1,j_1,k_1)$, $x_2 = (i_2,j_2,k_2)$, and $d(x_1,x_2)$ be the l_p distance on R^3. Sometimes, there are computational advantages to using distance functions other than the common Euclidean distance (l_2). Besides the fact that all metrics on a finite dimensional space are equivalent (16), certain exact variance estimates are tractable and computationally feasible. Suppose $\text{Cov}(D_{x_1}, D_{x_2}) = \sigma_D^2 \rho^{d(x_1,x_2)}$, where, as before, ρ is a measure of the smoothing autocorrelation kernel. This covariogram is, in fact, valid; that is, it is positive definite and induced by a legitimate Gaussian probability (see Appendix). If the domain of D is a cube (square is 2D) of size n, then the total number of voxels in Dom(D) is $n_{\text{tot}} = n^3$ ($n_{\text{tot}} = n^2$ in 2D) and

$$\begin{aligned}\widehat{\sigma_{\overline{D}}^2} &= \text{Var}(\overline{D}) = \text{Var}\left(\frac{1}{N \times n_{\text{tot}}} \sum_{\substack{x \in \text{Dom}(D) \\ 1 \le l \le N}} D_l(x)\right) \\ &= \frac{1}{n_{\text{tot}}^2} \sum_{x_1 \in \text{Dom}(D)} \sum_{x_2 \in \text{Dom}(D)} \text{Cov}[D_1(x_1), D_1(x_2)] \\ &= \frac{1}{n_{\text{tot}}^2} \left(n_{\text{tot}} \widehat{\sigma_D^2} + \sum_{x_1, x_2 \in \text{Dom}(D), x_1 \ne x_2} \widehat{\sigma_D^2} \rho^{d(x_1,x_2)} \right)\end{aligned} \tag{1}$$

Define

$$A = \sum_{x_1, x_2 \in \text{Dom}(D), x_1 \ne x_2} \widehat{\sigma_D^2} \rho^{d(x_1,x_2)}$$

then one can derive explicit closed forms for $\text{Var}(\overline{D})$ in 2D and 3D in the case of rectangular-type partitioning, in terms of n_{tot} and ρ (17). In 2D under the l_1 metric, A_2 ($= A$) can be expressed as

$$\begin{aligned}A_2 = 4\widehat{\sigma_{\overline{D}}^2} \Bigg(&\left[\frac{\rho(n-1)}{1-\rho} - \rho^2 \frac{1-\rho^{n-1}}{(1-\rho)^2} \right]^2 \\ &+ n \left[\frac{\rho(n-1)}{1-\rho} - \rho^2 \frac{1-\rho^{n-1}}{(1-\rho)^2} \right] \Bigg)\end{aligned} \tag{2}$$

The corresponding explicit formula in 3D case (cubical search region) for $\widehat{\sigma^2_{\overline{D}}} = \phi(\rho)$ is

$$\phi(\rho) = \widehat{\sigma^2_{\overline{D}}} = \frac{1}{n^2_{\text{tot}}}\left(n_{\text{tot}}\widehat{\sigma^2_D} + A_3\right) \tag{3}$$

where

$$A_3 = \widehat{\sigma^2_D}\left(2^3\left[\frac{\rho(n-1)}{1-\rho} - \rho^2\frac{1-\rho^{n-1}}{(1-\rho)^2}\right]^3 + 3n2^2\left[\frac{\rho(n-1)}{1-\rho} - \rho^2\frac{1-\rho^{n-1}}{(1-\rho)^2}\right]^2 + 3n^2 2\left[\frac{\rho(n-1)}{1-\rho} - \rho^2\frac{1-\rho^{n-1}}{(1-\rho)^2}\right]\right)$$

For more complex regions, such closed mathematical expressions of the variance estimates are not available. In this case, one writes

$$\widehat{\sigma^2_{\overline{D}}} = \text{Var}(\overline{D}) = \text{Var}\left(\frac{1}{N \times n_{\text{tot}}}\sum_{\substack{x\in \text{Dom}(D)\\ 1\le l\le N}} D_l(x)\right)$$

$$= \frac{1}{N^2 \times n^2_{\text{tot}}}\sum_{\substack{x_1\in \text{Dom}(D)\\ 1\le l_1\le N}}\sum_{\substack{x_2\in \text{Dom}(D)\\ 1\le l_2\le N}} \text{Cov}[D_{l_1}(x_1), D_{l_2}(x_2)]$$

$$= \frac{1}{n^2_{\text{tot}}}\left(\sum_{x_1,x_2\in \text{Dom}(D)} \widehat{\sigma^2_D}\,\rho^{d(x_1,x_2)}\right)$$

$$= \frac{1}{n^2_{\text{tot}}}\left(\sum_{k=0}^{\text{diam}(D)} \widehat{\sigma^2_D}\,\rho^k P_k\right) = \widehat{\sigma^2_D}\left(\frac{1}{n^2_{\text{tot}}}\sum_{k=0}^{\text{diam}(D)} \rho^k P_k\right)$$

where $P_k = |\{(x_1,x_2)\colon x_1,x_2 \in \text{Dom}(D),\ d(x_1,x_2) = k\}|$ and $\text{diam}(D) = \max\{d(x_1,x_2)\colon x_1,x_2 \in \text{Dom}(D)\}$ is the usual diameter of the subvolume D. There seems to be no simple closed form for the factors P_k for an arbitrary region D. Also, for computational purposes, it is not feasible to do an exhaustive search throughout the domain of D. In our tests, we have used stochastic approximations of $P_k, \forall k$ (under l_2 and l_1 distances) that yield stable estimates. For a structural probabilistic partitioning, our stochastic algorithm selects random voxel locations, within each ROI, according to the associated prior probability map. We define the expressions

$$CF = \frac{1}{n^2_{\text{tot}}}\sum_{k=0}^{\text{diam}(D)} \rho^k P_k$$

as *correction factors*. These are scaling factors needed to estimate $\widehat{\sigma^2_D}$, $\widehat{\sigma_{\overline{D}}} = \widehat{\sigma_D}\,(CF)^{1/2}$.

Because $D_x \sim N(0,\sigma^2_D)$, $\forall x$, and $\overline{D} \sim N(0,\sigma^2_{\overline{D}})$, we standardize $\overline{D}$ to determine, using a z test, whether activation occurs within the whole (sub)domain D. As a result, only if the test statistic (under the null hypothesis H_0: $\mu_D = 0$)

$$z = \frac{\overline{D}}{\widehat{\sigma_D}}$$

is large enough will we search through D voxel by voxel to determine the location(s) of the activation site(s). For this, we use t or z tests, as we described previously.

The simulated correction factors for all ROIs are uniformly bigger than their exact counterparts; however, their errors are all within 1%. Table 1 contains the values of both types of estimates of the CFs for the nine ROIs rescaled by a factor of 10^6. Here, the random search picked 1 of 1,000 voxels.

The above technique for determining the significant regions of activation allows variable thresholding of functional data on different anatomical regions of the brain defined within the probabilistic atlas. In general, the activation sites found by this method may not be present on a simple globa t statistic image, nor will all of the (uniform) t statistic voxels appear among the activation sites determined by the SVT technique.

RESULTS

We applied the SVT technique to identify and statistically analyze the differences in a left versus right finger-tracking subtraction paradigm under visual stimulus. The goal of the study was to map, using an underlying probabilistic brain atlas, the effects of the finger movement motor task on cerebral perfusion and identify the regions of the brain that exhibit significant variability related to this sensorimotor paradigm. Given the well documented basis of this simple visuomotor task, we demonstrate the validity of SVT in identifying the motor strip activation, in Brodmann area 4, associated with each task.

Let $\{X^1_l\}^6_{l=1}$ contain the PET data for the six subjects scanned under the right-hand finger-tracking task. Let $\{X^2_l\}^6_{l=1}$ contain the PET signals taken during the opposite left-hand motor task. Table 2 contains the results of the global tests for overall significance of the activa-

TABLE 1. *Stochastic estimates versus exact values of correction factors (CFs)*

CF evaluation	Region of interest								
	Cerebellum	Frontal	Occipital	Parietal	Temporal	Insula	Thalamus	Caudate	Putamen
Stochastic estimate of CF	665	274	773	446	533	4,089	5,461	5,010	5,858
Exact estimate of CF	661	272	766	443	529	4,052	5,411	4,980	5,803

TABLE 2. *Subvolume thresholding global statistical tests on subtraction paradigm for "finger-tracking" study*

	Region of interest								
Statistic	Cerebellum	Frontal	Occipital	Parietal	Temporal	Insula	Thalamus	Caudate	Putamen
Global z score	—	19.14	12.46	12.33	0.71	3.03	2.87	5.75	2.98

A high z score indicates that there are significant group diffrences between left- and right-hand motor tasks over the particular region of interest.

tion in the entire ROIs. We see that all ROIs are globally activated except the temporal lobe. Note that the cerebellum was excluded from this study due to data truncation in this region. The results of the second (local) SVT statistical testing identified the locations of the significant group differences in this subtraction paradigm (Fig. 3). Axial, coronal, and sagittal views of the statistically significant perfusion for the "left-right" (L-R) and "right-left" (R-L) contrasts are depicted in Fig. 3. As expected, the first subtraction activates the subjects' right premotor and motor cortex. The "right-left" contrast exhibits significant activation in the subjects' left motor cortices.

Table 3 contains the Talairach coordinates and the corresponding z scores of the centers of activation, in the primary motor cortex, as shown in Fig. 3. Positive and negative z scores correspond to positive and negative contrasts (i.e., L-R and R-L) for the "left-right" finger-tracking task, respectively.

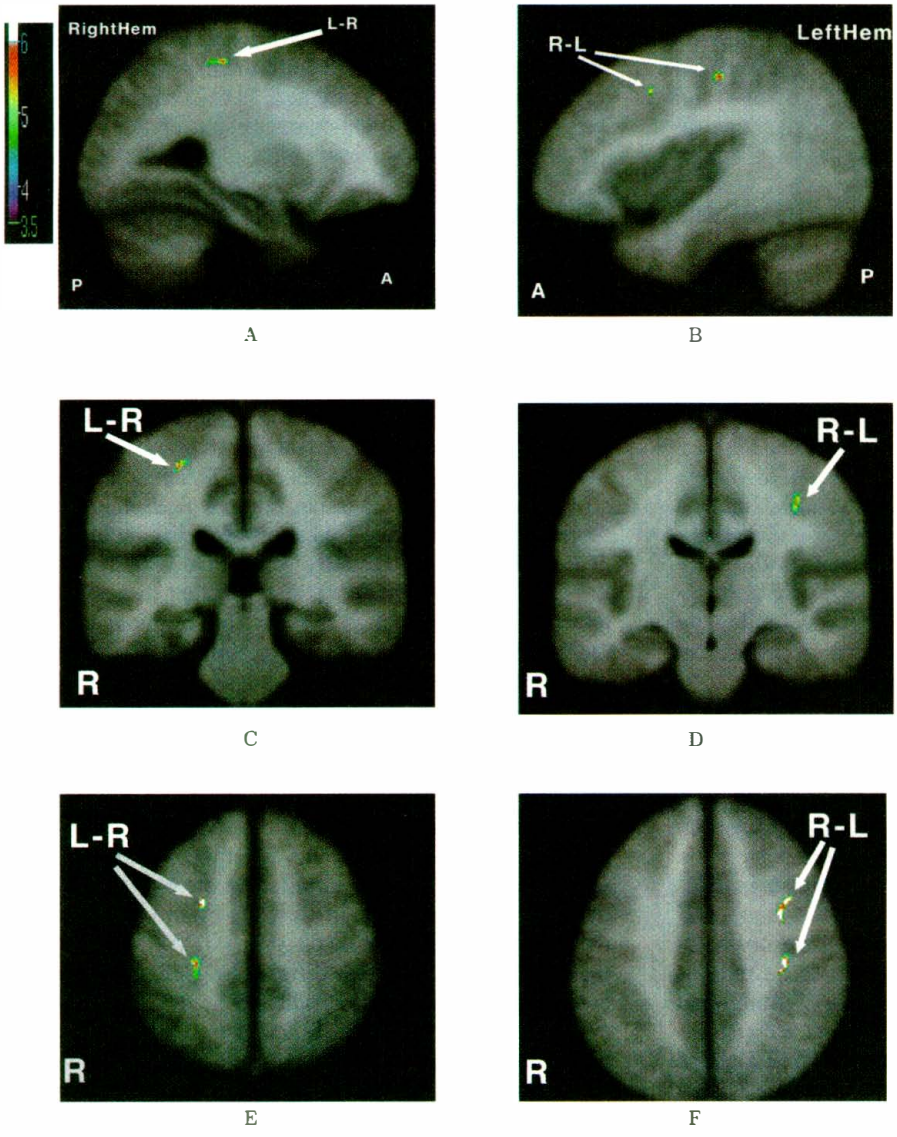

FIG. 3. Sagittal, coronal, and axial views of the subvolume thresholding (SVT) statistical significance difference maps comparing left- versus right-hand finger-tracking task. Images **A** and **B** show the right and left hemispheres and the SVT maps for the left minus right hand (L-R) and right minus left hand (R-L) paradigms, respectively. Coronal views of the same activation differences are shown in images **C** and **D**. Bilateral simultaneous activations of the premotor and the primary motor cortices for the two contrasts (L-R and R-L) are illustrated in transverse views on the bottom two images, **E** and **F**.

TABLE 3. *Talairach coordinates of centers of activation and corresponding z scores for some regions depicted in Fig. 3*

Area	Talairach coordinate			z scores
	x	y	z	
Left motor (4)	−33	−26	40	6.7
Left premotor (6)	−34	1.5	36	22.0
Right motor (4)	29	−28	48	6.3
Right premotor (6)	24	1	48	7.0

DISCUSSION AND CONCLUSIONS

We introduce and validate the SVT technique for statistical analysis of multisubject functional data within a probabilistic anatomic atlas using a simple sensorimotor paradigm. We employed the anatomically subdivided ICBM probabilistic atlas to constrain our analysis. Following this partitioning step, two types of statistical tests were applied. The first separates the SVT method from other techniques of functional statistical analysis and is aimed at determining the global significance of the differences between two groups over each search region separately. Depending on the anatomical structure and topology of a subvolume of interest, we determine an estimate for the pooled variance of the average across subjects and voxels. These estimates are then used to assess the globally significant variability of the data within each ROI.

The second step in statistical testing maps locally the voxels of significant functional group differences in each globally activated ROI. This is a standard procedure in most techniques for functional statistical mapping. SVT differs from other appraoches in two ways: First, voxel location tests are run only over the search regions of high significance levels according to the first global test results, and second the variance estimates are pooled over subjects and across voxels (longitudinally-meridianally).

In the SVT model, morphological and spatial registration differences between any two functional data sets are accounted for by using a probabilistic atlas that associates a probability value to each voxel to accommodate anatomic variability and registration error. Further, we analyze separate ROIs in the difference image for activation using different stationary random field models and thus avoid the problem of nonuniform global activity and signal variance within the brain.

The SVT method has three major assumptions: The difference images represent locally stationary random fields with Gaussian autocorrelation; the autocorrelation of two voxel intensities in two different subjects is independent of the order of the subjects within the group; and (difference) image intensities at each voxel are normally distributed. These assumptions are shown to be reasonable theoretically (based on the physics of functional imaging and the algorithms for PET image reconstruction) and empirically using real PET data. One drawback of the SVT method is that it uses the standardized mean to estimate global significance over ROIs. The presence of positive and negative activation within an ROI may cause false-positive error. In practice, however, our experiments (motor, education, and drug treatment subtraction studies) show that this is rarely the case because the probabilistic anatomic partition of the brain is driven by the anatomic question of the functional study.

There are at least two other major approaches for dealing with statistical mapping of functional brain data. The first one contains various multivariate techniques (18), where one obtains global statistical inference on the multivariate statistic over the entire brain but voxel-based analysis is not feasible (due to the number of voxels greatly exceeding the number of scans). Second are the univariate approaches. The most widely used univariate scheme is statistical parametric mapping (SPM) (19). SPM makes use of the general linear model, which includes localized t testing and linear regression and thus is more universally applicable for a variety of image modalities (PET, SPECT, functional MRI) and activation paradigms (subtractive, parametric, factorial) and a wider range of hypothesis testing. The SVT method, on the other hand, is more specialized for subtraction studies involving only PET and SPECT data. Whereas the SPM approach employs Worsley et al.'s (12) formulas for the expectation of the Euler characteristic of the excursion set above a given threshold value, a generalization of the theory of Gaussian field level crossing (15), the SVT relies on an intuitive and computationally attractive type of skew-Bonferroni correction for the large number of tests using nonindependent univariate statistics. Instead of fixing a p value and determining an appropriate threshold value for our statistical maps, we declare statistically significant the voxel locations where the univariate statistics exceed the threshold associated with the p value of $0.05/|I|$, where $|I|$ is the number of uncorrelated voxels within each ROI. This way, we avoid the problem of having to transform the observed t statistical image to an approximate 3D Gaussian random field using a univariate transformation. This approximation requires high degrees of freedom (usually ≥ 30) (19), which is rarely the case in PET/SPECT studies. Another distinction betwee the two methods is the fact that regional ROI statistical inferences are available through the SVT approach that are induced by the underlying anatomic probabilistic brain atlas. We consider a more general Gaussian field model where stationarity is imposed only locally within each ROI, and thus different subvolumes can, and oftentimes do, have quite different distribution parameters (means, variances).

Empirical evidence for the differences between SPM and SVT is provided by comparing the two methods on the PET data discussed in Results. Figure 4 shows two axial views of the SPM maps ($p = 0.025$), which clearly indicate significant group differences (left- versus right-hand finger tracking) in Brodmann areas 4 and 6. However, there are also significant differences present in white matter and CSF regions.

We have also compared the SVT maps for this motor study with a uniform thresholding at level 2.5%. Uni-

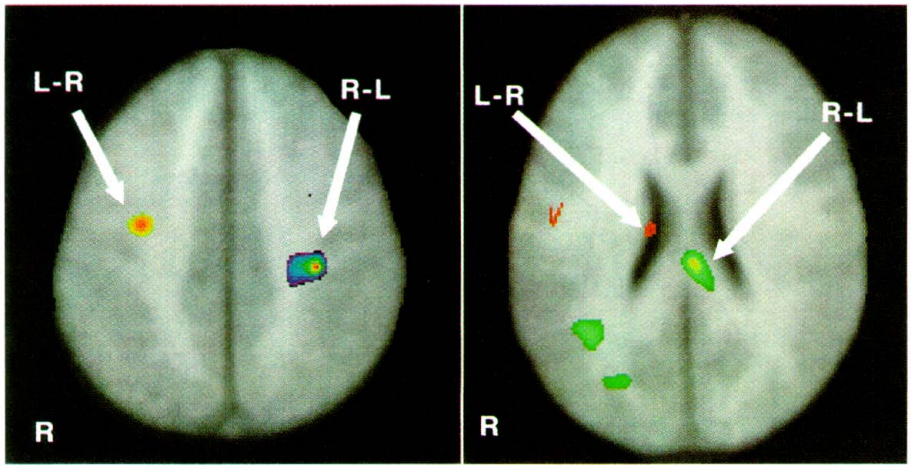

FIG. 4. Axial views of the statistical parametric mapping statistical maps, illustrating significant right- versus left-hand finger-tracking differences. The right image shows group differences in the corpus callosum and the ventricles (arrows).

form thresholding at a level t represents the top t% of the average difference intensity at each voxel. In other words, all voxel intensities are set to zero except the ones where the average diffrence is in the top t%. Figure 5 illustrates in axial and sagittal views the bilateral motor strip and the left temporal lobe (z score 2.1) activations in the uniform (2.5%) statistical maps. Recall that according to the SVT regional ROI statistics (Table 2), the group differences between the left- and right-hand paradigm are insignificant in the entire temporal lobe.

In summary, SPM, uniform (2.5%), and SVT all correctly identify the paradigm-specific statistically significant group differences (left and right motor cortex) between the left- and right-hand finger-tracking tasks. However, due to implicit foundational differences between these techniques (e.g., variance estimates, assumptions of global stationarity), there are fine empirical variations in the corresponding statistical significance maps.

APPENDIX

Theoretical and Empirical Evidence in Support of SVT Hypotheses

We now show theoretically, using the physical properties of the imaging process, and empirically, using plots of real PET data, that the hypotheses we make in our SVT model are reasonable.

If we place a single point source of radioactive isotope in the center of a PET camera, the image we obtain looks smeared due to low pass filter processing (14) (see Fig. 6). The smoothing kernel has a bell shape and can be modeled by a 2D normal distribution. There are two main reasons for observing (Gaussian) smooth PET images: The first is the physiology of brain function: Blood flow or metabolic change occurs smoothly and homogeneously. The second is the stochastic nature of the path

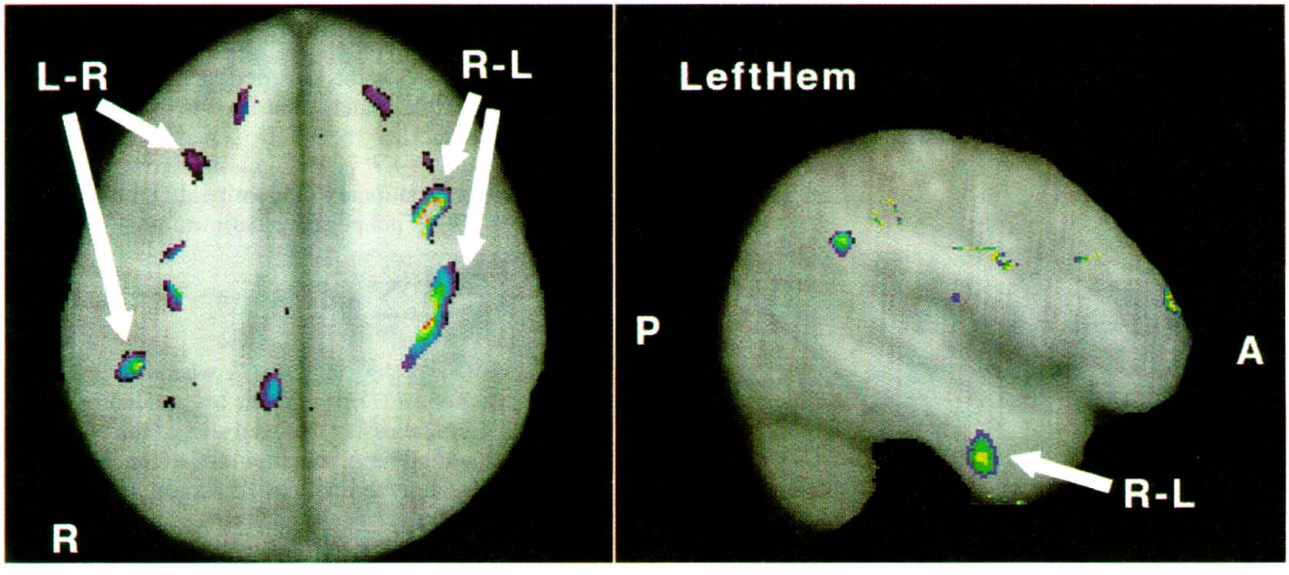

FIG. 5. Axial and sagittal views of the uniform (2.5%) statistical maps, illustrating significant right- versus left-hand finger-tracking differences in areas 4 and 6 and the temporal lobe.

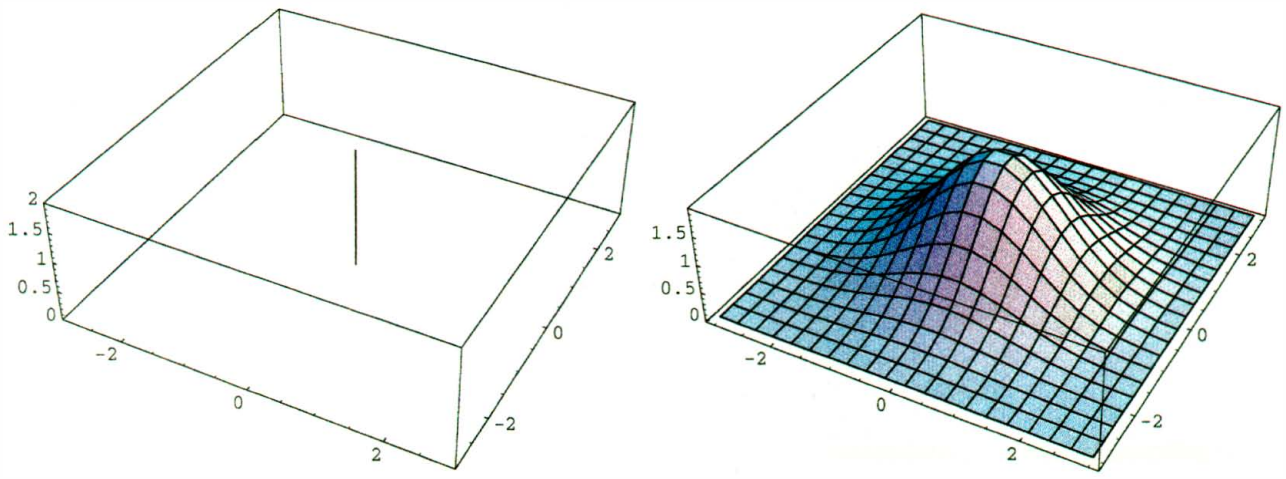

FIG. 6. Spatial Gaussian voxel intensity correlation point source isotope data **(left)** and observed image **(right).**

of the positively charged β particles (from their emission from the nucleus to their collision with negatively charged electrons) and the attenuation effects causing nearby voxels to have highly positively correlated intensities. Coupling every detector in the PET scanner with several other detectors in the neighborhood of its 180° opposite also introduces a distance-dependent autocorrelation function similar to a Gaussian distribution.

To explain the rationale behind the assumption of a normal distribution of voxel intensities, we again refer to the physics of PET imaging. A PET scan is constructed by detecting, comparing (times/places of arrival), and counting dual photons emitted in the process of positron-electron annihilation. Photon strikes can be regarded as random arrivals and modeled as a discrete Poisson process. Because of the large scale of this stochastic process, its distributioin can be approximated by a Gaussian (of mean zero and some unknown variance) (17). Empirically, we demonstrate the normal structure of the voxel intensities by taking 500 randomly selected intensities (that are far enough from each other and are not significantly correlated) of a difference image. Figure 7 shows the values of the differences on the left and the quantiles of a normal distribution (having the sample mean and variance of the difference data) on the right. The almost linear relation of the data and the normal quantiles suggests that the sample was drawn from a (unknown) distribution closely related to normal. A Kolmogorov-Smirnov (KS) normality test (20) provides an additinal quantitative argument to this effect. We applied a two sample KS test to a PET volume representing the difference of the two scans of the same subject under the identical functional paradigm: right-hand finger-tracking task with LED stimulus in the subject's right visual field. All PET data are in ICBM space (1). Using Splus, we compared the distribution of 500 not-sufficiently correlated difference voxel intensities (farther than 15 mm apart) with a sample of 500 $N(0, 1)$ normally distributed random variables. The KS score of 0.058 and the corresponding probability value of 0.3406 indicated that indeed the observed data can be assumed to be Gaussian.

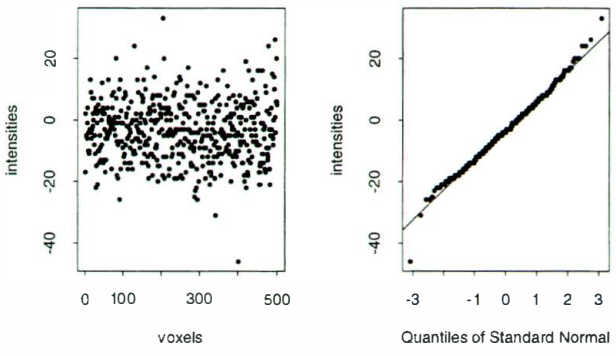

FIG. 7. Normal nature of voxel intensities: 500 randomly chosen (uncorrelated) differences **(left)** and sample/normal quantiles plot **(right).**

A Class of Valid Covariance Models

We now show that the covariogram we adopted and used is permissible (valid); that is, it is underlined by a legitimate probability model. In general, a continuous function $c(h)$: $R^n \to R$ is an admissible covariance (covariogram) for a stationary random field D_x on R^n (15) if and only if $c(h)$ is nonnegative definite,[2] that is,

$$\sum_{k=1}^{n}\sum_{l=1}^{n} \alpha_k \overline{\alpha}_l c(x_k - x_l) \geq 0$$

for all $\alpha = (\alpha_1, \alpha_2, \cdots, \alpha_n)^t \in C^n$, where $c(x_k - x_l) = \mathrm{Cov}(D_{x_k}, D_{x_l})$ and $E(D_x) = \mu$, $\forall x$ by stationarity.

In 1984 Christakos (21) proved the validity of large classes of covariogram/variogram models, including the case of $K\rho^{\|h\|_2^2}$ using the Euclidean distance. To verify the validity of the covariance model $c(h) = K\rho^{\|h\|_p^p}$ for any

[2]The "bar" notation, $\bar{}$, indicates complex conjugation throughout this section.

positive integer p, we need the following spectral theory fact (22). If the Fourier transform of an L_1 function, $c(h)$, is a nonnegative L_1 function $c(w)$, then $c(h)$ is nonnegative definite.

To see the reason behind this result, choose $c(h) \in L_1(R^n)$ whose Fourier transform exists and $FT(c)(w) = \hat{c}(w) = \int_{R^n} c(h)e^{-2\pi i<w,h>}dh$, then $c(h) = \int_{R^n} e^{2\pi i<w,h>}\hat{c}(w)dw$ (16). Therefore,

$$c(x_k - x_l) = \int_{R^n} e^{2\pi i(<w,x_k>-<w,x_l>)}\hat{c}(w)dw$$

Expanding the quadratic form,

$$\sum_{k=1}^{n}\sum_{l=1}^{n} a_k\overline{a}_l c(x_k - x_l)$$

$$= \sum_{k=1}^{n}\sum_{l=1}^{n}\left(a_k\overline{a}_l \int_{R^n} e^{2\pi i(<w,x_k>-<w,x_l>)}\hat{c}(w)dw\right)$$

$$= \int_{R^n}\sum_{k=1}^{n}\sum_{l=1}^{n}[a_k e^{2\pi i<w,x_k>}\,\overline{a}_l e^{-2\pi i<w,x_l>}\hat{c}(w)]dw$$

$$= \int_{R^n}\left|\sum_{l=1}^{n} a_l e^{2\pi i<w,x_l>}\right|^2 \hat{c}(w)dw \geq 0$$

The last inequality follows from the assumption that the Fourier transform of $c(h)$ is nonnegative.

We also need to argue that if $\|\bullet\|_1$ is the l_1 norm on R^3, ($\|h\|_1 = |h_1| + |h_2| + |h_3|$), then the function $c(h) = K\rho^{\|h\|_1}$, $0 < \rho < 1$, induces a valid covariance functional

$$\mathrm{Cov}(D_{x_1}, D_{x_2}) = C(x_1, x_2) = c(x_1 - x_2)$$

$$= c(h) = K\rho^{\|h\|_1} = K\prod_{k=1}^{3}\rho^{|h_k|}$$

for any positive constant K (in our models, we have used $K = \sigma_D^2$).

We look at the Fourier transform

$$FT(c) = \hat{c}(w) = \int\int\int_{R^3} c(h)e^{-2\pi i<h,w>}dh$$

$$= K\left(\int_R \rho^{|h_1|}\, e^{-2\pi i h_1 w_1}\, dh_1\right)$$

$$\left(\int_R \rho^{|h_2|} e^{-2\pi i h_2 w_2}\, dh_2\right)\left(\int_R \rho^{|h_3|} e^{-2\pi i h_3 w_3}\, dh_3\right)$$

$$= K\prod_{k=1}^{3}\int_R \rho^{|h_k|} e^{-2\pi i h_k w_k} dh_k$$

$$= K\prod_{k=1}^{3}\int_R e^{|h_k|\ln(\rho)} e^{-2\pi i h_k w_k} dh_k$$

$$= 2K\prod_{k=1}^{3}\frac{a}{a^2 + b_k^2} \geq 0$$

where $a = -\ln(\rho)$ and $b_k = 2\pi w_k$. Further, $\|\hat{c}(w)\|_1 < \infty$. The last equality follows from the fact that an integral of an odd function on a symmetric interval is zero. Therefore, if a is a constant,

$$\int_R e^{-|x|a}e^{-2\pi i x w}dx = \int_R e^{-|x|a}[\cos(2\pi x w) - i\sin(2\pi x w)]dx$$

$$= 2\int_0^\infty e^{-|x|a}\cos(2\pi x w)dx$$

$$= 2\frac{a}{a^2 + (2\pi w)^2}$$

Therefore, we see that the covariogram induced by the continuous function $c(h) = K\rho^{\|h\|_1}$ is indeed permissible.

Observe, also, that similar approaches could be used to show that any l_p norm on R^n would induce an admissible covariogram model of the type $c(h) = K\rho^{\|h\|_p^p}$. In addition, having that $c(h)$ is valid on R^n implies that it is also valid on R^{n-k}, for $0 \leq k < n$ (21,23).

Acknowledgment: Grant support for this work was provided by an NIA award K08AG100784 (M.S.M.), the Howard Hughes Institute, Fullbright Commission, and grant no. G-1-00001 of the U.S. Information Agency (P.M.T.); Human Brain Project (NIMH/NIDA: P20MH/DA 52176), NLM (LM/MH05639), NINDS (NS 38753), and NCRR (RR 13642) (A.W.T.); and NSF DMS-9403454 and NIH P20 MH57180 (I.D.D. and D.W.L.S.).

REFERENCES

1. Mazziotta JC, Toga AW, Evans AC, Fox P, Lancaster S. A probabilistic atlas of the human brain: theory and rationale for its development. *Neuroimage* 1995;2:89–101.
2. Talairach J, Tournoux P. Principe et technique des etudes anatomiques. In: Rayport M, ed. *Co-planar stereotaxic atlas of the human brain—3-dimensional proportional system: an approach to cerebral imaging*. New York: Thieme Medical, 1988:3–9.
3. Evans AC, Collins DL, Holmes CJ. *Automatic 3D regional MRI segmentation and statistical probabilistic anatomical maps*. New York: Academic Press, 1996:123–130.
4. Mega MS, Thompson PM, Cummings JL, et al. Sulcal variability in the Alzheimer's brain: correlations with cognition. *Neurology* 1998;50:145–51.
5. Thompson P, Schwartz C, Lin RT, Khan AA, Toga A. Three-dimensional statistical analysis of sulcal variability in the human brain. *J Neurosci* 1996;16:4261–74.
6. Thompson PM, MacDonald D, Mega MS, Holmes CJ, Evans AC, Toga AW. Detection and mapping of abnormal brain structure with a probabilistic atlas of cortical surfaces. *J Comput Assist Tomogr* 1997;21:567–81.
7. Thompson P, Schwartz C, Lin RT, Khan AA, Toga A. Three-dimensional statistical analysis of sulcal variability in the human brain. *J Neurosci* 1996;16:4261–74.
8. Friston KJ, Frith CD, Liddle PF, Dolan RJ, Frackowiak RSJ, Lammertsma AA. The relationship between the global and local changes in PET scans. *J Cereb Blood Flow Metab* 1990;10:458–66.
9. Woods RP, Cherry SR, Mazziotta JC. Rapid automated algorithm for aligning and reslicing PET images. *J Comput Assist Tomogr* 1992;16:620–33.
10. Worsley K. Quadratic tests for local changes in random fields with applications to medical images. Technical report, Dept. of Math and Statistics, McGill University, Canada, August 1994.

11. Woods RP, Mazziotta JC, Cherry SR. MRI-PET registration with automated algorithm. *J Comput Assist Tomogr* 1993;17:536–46.
12. Worsley K, Evans AC, Marrett S, Neelin P. A three-dimensional statistical analysis for CBF activation studies in human brain. *J Cereb Blood Flow Metab* 1992;12:900–18.
13. Antoine MJ, Trevére JM, Bloyet D. Modeling of 2D PET noise autocovariance function applied to individual activation studies. IEEE Medical Imaging Conference, Norfolk, VA, U.S.A., 1994;4:1628–32.
14. Worsley K, Marrett S, Neelin P, Evans AC. Searching scale space for activation in PET images. *Hum Brain Map* 1996;4:74–90.
15. Adler R. *The geometry of random fields.* New York: Wiley, 1981.
16. Folland G. *Real analysis: modern techniques and their applications.* New York: Wiley, 1984.
17. Dinov ID. Mathematical and statistical techniques for modeling and analysis of medical data. Ph.D. thesis, Florida State University, ATTN: Interlibrary Loan Service, Dirac Science Library, Florida State University, Tallahassee, Florida 32306. Tel: (850) 644-2202. UMI Dissertation Services, 300 North Zeeb Rd, Ann Arbor, MI 48106-1346. Tel: (800) 521-0600. The cost is $41.50., 1998.
18. Friston KJ, Poline JP, Strother S, Holmes AP, Frackowiak RSJ, Frith CD. A multivariate analysis of PET activation studies. *Hum Brain Map* 1996;4:140–51.
19. Friston KJ, Holmes AP, Worsley KJ, Poline J-P, Frith CD. Frackowiak RSJ. Statistical parametric maps in functional imaging: a general linear approach. *Hum Brain Map* 1995;2:189–210.
20. Smirnov NV. Table for estimating the goodness of fit of empirical distributions. *Ann Math Stat* 1948.
21. Christakos G. On the problem of permissible covariance and variogram models. *Water Resources Res* 1984;20:251–65.
22. Bochner S. *Lectures on Fourier integrals.* Princeton: Princeton University Press, 1959.
23. Cressie N. *Statistics for spatial data.* New York: Wiley, 1991.